

7.2.5. Instantaneous Total Drag Under Accelerating Subsonic Flow

To supplement the preliminary aerodynamic analysis, an unsteady CFD study was conducted using open source CFD code OpenFOAM and Paraview to evaluate the instantaneous total drag response of both rocket configurations under accelerating subsonic flow. The objective was to examine the time-dependent drag behavior during the early phase of freestream acceleration.

7.2.5.1. Problem Definition

This analysis examines the instantaneous aerodynamic drag response of two rocket vehicle configurations subjected to an accelerating subsonic freestream. The objective is to isolate and characterize drag behavior arising solely from unsteady freestream acceleration, independent of vehicle motion or attitude changes. Two geometrically distinct vehicle configurations are analyzed. Each configuration is modeled as a rigid, full three-dimensional body immersed in an external flow. The vehicles differ in geometry and surface features, resulting in different aerodynamic drag characteristics under identical flow conditions.

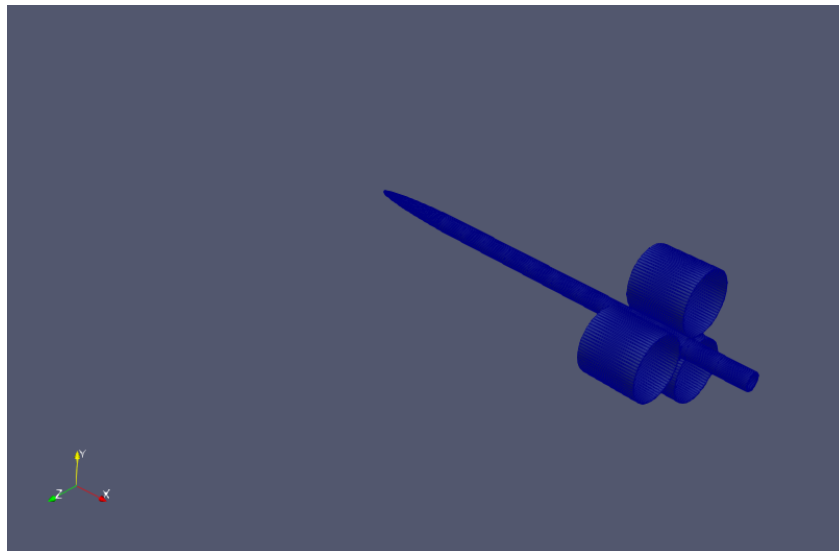


Fig. 7.17. Rendered Geometry of Altitude Vehicle

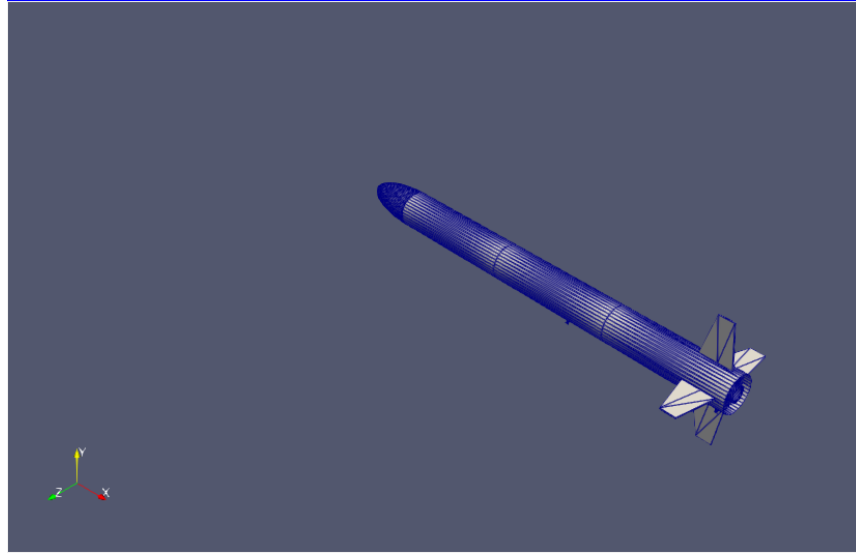


Fig. 7.18. Rendered Geometry of Mars Rover Vehicle

To constrain the flow field to remain within the fully subsonic regime throughout the simulation:

- Freestream Mach number increases smoothly with time
- No transonic effects or shock formation are present
- Compressibility effects are included but remain continuous and smooth

This regime ensures that unsteady drag variations are driven by acceleration-induced flow development rather than shock-related phenomena.

The following assumptions define the physical model and scope of the problem:

- Subsonic flow only. No shocks or shock-induced drag components
- Fixed vehicle orientation throughout the simulation
- Rigid body assumption (no structural deformation)
- No angle-of-attack variation
- Freestream acceleration imposed through inlet boundary conditions

The vehicle remains stationary in the computational domain, and all unsteady aerodynamic effects arise exclusively from the time-dependent freestream velocity. The sole aerodynamic quantity investigated in this study is instantaneous total drag, decomposed into pressure drag contribution and viscous drag contribution. Drag is evaluated as a function of time during the acceleration phase, allowing direct assessment of transient drag behavior under non-steady flow conditions.

7.2.5.2. Physical/Mathematical Model

The aerodynamic flow field is modeled using a time-accurate, compressible Unsteady Reynolds-Averaged Navier-Stokes (URANS) formulation. The objective is to resolve the unsteady evolution of aerodynamic drag induced by freestream acceleration under fully subsonic conditions.

The compressible URANS equations consist of the conservation laws for mass, momentum, and energy, written for Reynolds-averaged quantities.

7.2.5.2.1. Governing Equations

$$\frac{\partial \rho}{\partial t} + \nabla \cdot (\rho u) = 0 \quad \text{Eq. (1)}$$

$$\frac{\partial(\rho u)}{\partial t} + \nabla \cdot (\rho u \otimes u) = - \nabla p + \nabla \cdot \tau_{eff} \quad \text{Eq. (2)}$$

$$\tau_{eff} = \mu_{eff} [\nabla u + (\nabla u)^T - \frac{2}{3}(\nabla \cdot u)] \quad \text{Eq. (3)}$$

$$\frac{\partial(\rho t)}{\partial t} + \nabla \cdot (\rho ue) = - p \nabla \cdot u + \nabla \cdot (k_{eff} \nabla T) + \Phi \quad \text{Eq. (4)}$$

where ρ is the fluid density, u is the velocity vector, p is the static pressure, τ_{eff} is effective stress tensor, μ_{eff} is effective dynamic viscosity, T is the temperature, k_{eff} is the effective thermal conductivity, and Φ is the viscous dissipation term.

7.2.5.2.2. Thermophysical Model and Equation of State

The working fluid is modeled as a calorically perfect air gas formulation with constant thermophysical properties. The compressible flow formulation is closed using a temperature-dependent equation of state and constant transport and thermodynamic coefficients. The equation of state is defined as $p = \rho RT$ where p is the static pressure, ρ is density and R is the specific gas constant as a calorically perfect gas. Thermophysical properties are defined assuming constant specific heat at constant pressure $C_p = 100.5 \text{ J}\cdot\text{kg}^{-1}\cdot\text{K}^{-1}$ with a reference enthalpy $H_f = 0$. Viscous transport properties are assumed constant over the simulated temperature range, with dynamic viscosity $\mu = 1.82 \times 10^{-5} \text{ kg}\cdot\text{m}^{-1}\cdot\text{s}^{-1}$ and a Prandtl number $Pr = 0.71$. The energy equation is solved in terms of sensible internal energy, consistent with the calorically perfect gas assumption. Heat transfer at the rocket surface is modeled using an adiabatic wall condition, neglecting conductive heat flux through the solid body. This

thermophysical modeling approach is appropriate for the fully subsonic flow regime considered and ensures that compressibility effects are captured without introducing additional temperature dependent property variations.

7.2.5.2.3. Turbulence Model: $k - \omega$ SST

Turbulence effects are modeled using the Shear Stress Transport (SST) $k-\omega$ model, which blends the near-wall accuracy of the $k-\omega$ model with the free-stream robustness of the $k-\varepsilon$ formulation.

Turbulent Kinetic Energy k

$$\frac{\partial(\rho k)}{\partial t} + \nabla \cdot (\rho u k) = P_k - \beta^* \rho k \omega + \nabla \cdot [(\mu + \sigma_k \mu_t) \nabla k] \quad \text{Eq. (5)}$$

Specific Dissipation Rate ω

$$\frac{\partial(\rho \omega)}{\partial t} + \nabla \cdot (\rho u \omega) = \alpha \frac{\omega}{k} P_k - \beta \rho \omega^2 + \nabla \cdot [(\mu + \sigma_\omega \mu_t) \nabla \omega] \quad \text{Eq. (6)}$$

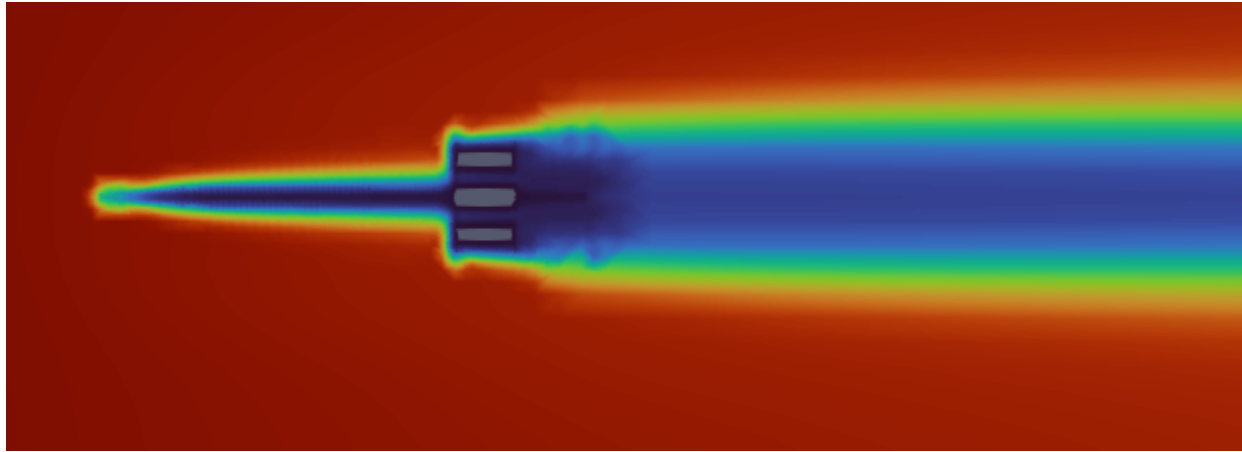


Fig. 7.19. Altitude Vehicle Turbulent Eddy-Viscosity Distribution

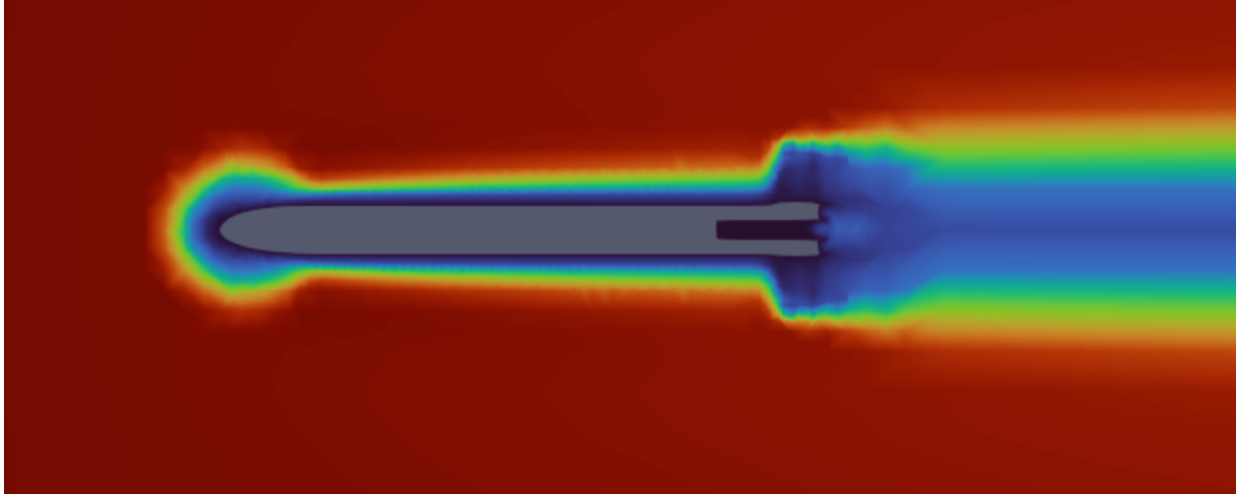


Fig. 7.20. Mars Rover Vehicle Turbulent Eddy-Viscosity Distribution

7.2.5.2.4. Unsteady Forcing Mechanism

Unsteady is introduced exclusively through the freestream velocity boundary conditions imposed at the inlet $U_{\infty}(t) = \min(U_{max}, \frac{U_{max}}{T_{ramp}} t)$. The time-dependent inlet velocity produced an accelerating flow field without altering vehicle orientation or geometry, isolating acceleration-induced aerodynamic effects.

7.2.5.2.5. Quantity of Interest: Total Drag

The instantaneous total drag force $D(t)$ is computed by integrating pressure and viscous stresses over the vehicle surface:

$$D(t) = \int_S [-pn + \tau_{eff} \cdot \hat{n}] \cdot \hat{x} dS \quad \text{Eq. (7)}$$

and the corresponding drag coefficient is defined as

$$C_D(t) = \frac{D(t)}{\frac{1}{2} \rho_{\infty} U_{\infty}^2 A_{ref}} \quad \text{Eq. (8)}$$

where A_{ref} is the reference area and the \hat{x} is the freestream direction.

7.2.5.3. Numerical Model

The governing equations are solved using a finite volume method (FVM) based OpenFOAM solver. Use of FVM ensures strict conservation of mass, momentum, and energy over each control volume and thus is well suited for compressible unsteady external flow.

7.2.5.3.1. Solver Description

The rhoPimpleFoam solver was used which is a density-based compressible flow solver designed for unsteady flow. The solver combines the PISO and SIMPLE algorithms through the PIMPLE framework, which allow robust pressure-velocity coupling for transient flows. Thus, this approach enables time accurate solutions while maintaining reasonable computational cost for URANS simulations.

7.2.5.3.2. Temporal Discretization

Time integration is performed using a first-order implicit Euler scheme that provides numerical stability for unsteady simulations involving accelerating flow conditions. To maintain stability and accuracy adaptive time stepping was enabled, Courant number was constrained to ≤ 0.7 , and a maximum allowable time step was imposed. This ensured transient drag variations were resolved without introducing excessive numerical dissipation.

7.2.5.3.3. Spatial Discretization

All spatial terms are discretized using finite volume surface integrals evaluated over cell faces.

- Gradient terms are computed using a Gauss linear scheme with cell-based limiting.
 - Convective terms are discretized using bounded upwind or linear-upwind schemes
 - Diffusive terms are discretized using second-order corrected Gauss schemes
- These choices balance numerical stability with sufficient accuracy.

7.2.5.3.4. Pressure-Velocity Coupling

Pressure-velocity coupling is handled through the PIMPLE algorithm with one outer corrector per time step and one non-orthogonal correction to account for mesh skewness. This ensures consistent coupling during unsteady acceleration.

7.2.5.3.5. Turbulence-Flow Coupling

Turbulence quantities are solved in a fully coupled manner with mean flow equations using the URANS framework. Turbulent transport equations for k and ω are discretized and integrated in time using the same finite volume approach as the mean flow equations. The URANS approach is appropriate for this problem because the flow remains in subsonic with no shock formation, the primary unsteadiness arises from freestream acceleration compared to turbulent resolving physics, and the objective is to capture time-dependent drag trends instead of instantaneous turbulent structures. Therefore, compared to Large-Eddy Simulation (LES)/Direct-Numerical Simulation(DNS) URANS provides an efficient and physically consistent framework for analyzing acceleration induced drag.

7.2.5.4. Computational Domain

Both vehicle configurations were simulated using a similar computational domain framework designed to minimize boundary interference while capturing wake development under subsonic accelerating flow. The computational domain is a rectangular box aligned with the freestream direction with extents defined relative to the vehicle reference diameter D (characteristic length):

- Upstream extent: 5D
- Downstream extent: 15D
- Lateral extents: 8D in both transverse directions

These dimensions ensure that inlet acceleration effects develop smoothly before reaching the vehicle and that wake structures contributing to drag are sufficiently resolved downstream. Boundary conditions were applied as follows:

- Inlet: Time-dependent velocity boundary condition imposing freestream acceleration
- Outlet: Pressure-based outlet allowing unsteady flow exit
- Farfield boundaries: Slip condition to minimize artificial shear
- Vehicle surface: No-Slip, adiabatic wall
-

7.2.5.4.1. Mesh Generation Strategy

Mesh generation for both vehicles follow the same overall strategy to ensure consistency in drag comparison. Background mesh was generated using blockMesh, a structured mesh generator. Geometry conforming mesh was generated using snappyHexMesh, an unstructured conforming mesh generator. Local refinement was applied on the vehicle bodies using surfaceFeatureExtract, an OpenFOAM refinement tool.

7.2.5.4.2. Mesh Quality Assessment

Mesh quality is verified using OpenFOAM's checkMesh utility. For both configurations, the following criteria were satisfied:

- Single connected region
- Acceptable non-orthogonality
- Acceptable skewness
- No illegal or inverted cells
- Adequate aspect ratios for URANS

7.2.5.4.3. Altitude Vehicle Mesh

The Altitude Vehicle mesh consists of approximately 815,000 cells.

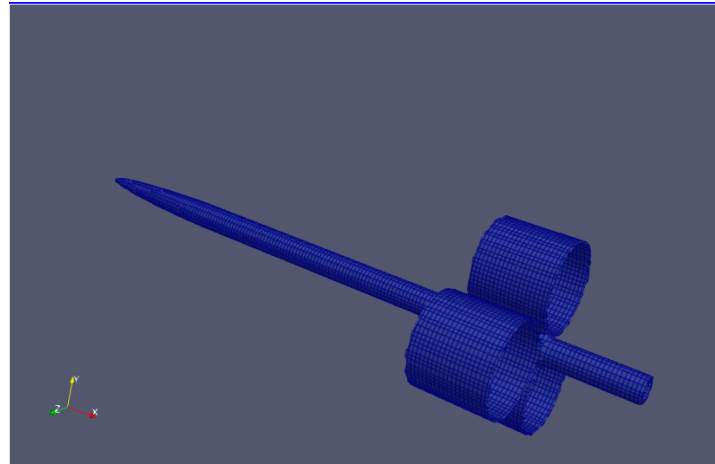


Fig. 7.21. Refined Mesh of Altitude Vehicle

7.2.5.4.4. Mars-Rover Vehicle Mesh

The Mars-Rover Vehicle mesh contains approximately 788,000 cells.

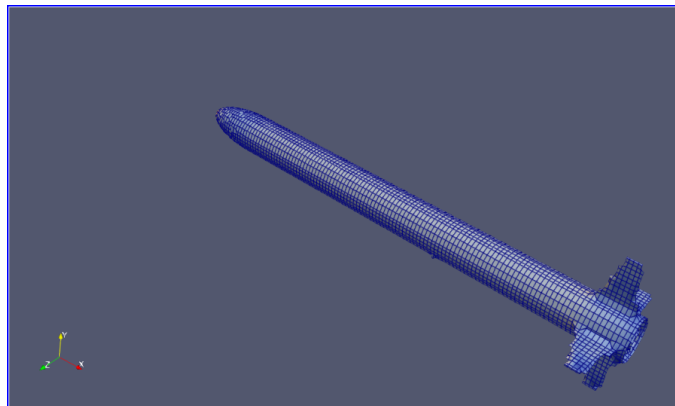


Fig. 7.22. Refined Mesh of Mars Rover Vehicle

7.2.5.5. Boundary/Initial Conditions

The boundary and initial conditions define the physical forcing mechanism of the simulation. In this analysis, unsteadiness is introduced through a time-dependent inlet velocity while all other boundaries are treated to minimize artificial reflections and constraint effects.

Table 7.7. Boundary Conditions

Boundary	Velocity (U)	Pressure (p)	Temperature (T)	Turbulence Variables
Inlet	Time-dependent (codedFixedValue)	Zero-gradient	Fixed value	Fixed values

Outlet	InletOutlet	Fixed value	Zero-gradient	Zero-gradient
Farfield	Slip	Zero-gradient	Zero-gradient	Zero-gradient
Vehicle surface	No-slip	Zero-gradient	Zero-gradient (adiabatic)	Wall functions

7.2.5.5.1. Boundary Condition Descriptions

Inlet: The inlet boundary prescribes the source of unsteadiness. A time-dependent velocity profile is imposed to generate a continuously accelerating freestream allowing the drag response to be evaluated under non-equilibrium flow conditions.

Outlet: The outlet boundary is treated to permit smooth flow exit from the domain while preventing artificial reflections that could contaminate the unsteady drag signal.

Fairfield: The farfield boundaries are configured to minimize confinement effects and allow the flow to adjust naturally to the impose acceleration without introducing spurious pressure or velocity gradients.

Vehicle surface: The vehicle surface enforces no-slip, adiabatic wall condition, ensuring that viscous shear stresses and pressure forces contributing to drag are physically resolved.

7.2.5.5.2. Initial Condition Description

All flow variables are initialized to uniform freestream values consistent with the initial inlet velocity. This provides a well defined starting point from which the unsteady flow development due to acceleration can be observed without introducing artificial transients.

7.2.5.6. Quantities of Interest

The objective of this analysis was to quantify the aerodynamic drag response of the vehicle during accelerating flow. Accordingly, post-processing is focussed exclusively on force based quantities that directly characterize drag and its physical contributors.

The following quantities are extracted from the URANS simulations:

Total drag coefficient $C_D(t)$: The instantaneous total drag acting on the vehicle as a function of time.

Pressure drag coefficients $C_{D,p}(t)$: The component of drag arising from surface pressure forces.

Viscous drag coefficient: $C_{D,v}(t)$: The component of drag arising from wall shear stresses.

Drag quantities are evaluated instantaneously in time during the accelerating portion of the flow. Since the freestream velocity varies continuously, the resulting drag response is inherently unsteady and does not correspond to a steady equilibrium state at any given Mach number. This provides a direct measure of rate-dependent aerodynamic response, separation of pressure driven and viscous driven contributions, and insight into how drag evolves as the flow accelerates. In addition to the instantaneous values, the time averaged coefficients are computed over the interval [0, ~0.33] seconds. The time averaged quantities are used to challenge noise from data as it reduces sensitivity to short time numerical fluctuations and provides a single representative drag value for comparison between vehicles.

7.2.5.7. Instantaneous Drag Quantities

Instantenous aerodynamic drag response of each vehicle under accelerating subsonic flow is reported over the time interval $t = 0$ to $t = \sim 0.33$ seconds during which freestream velocity increases monotonically. All drag quantities are decomposed into pressure and viscous contributions to clarify the dominant drag mechanism during acceleration.

7.2.5.7.1 Drag Behavior Under Accelerating Flow

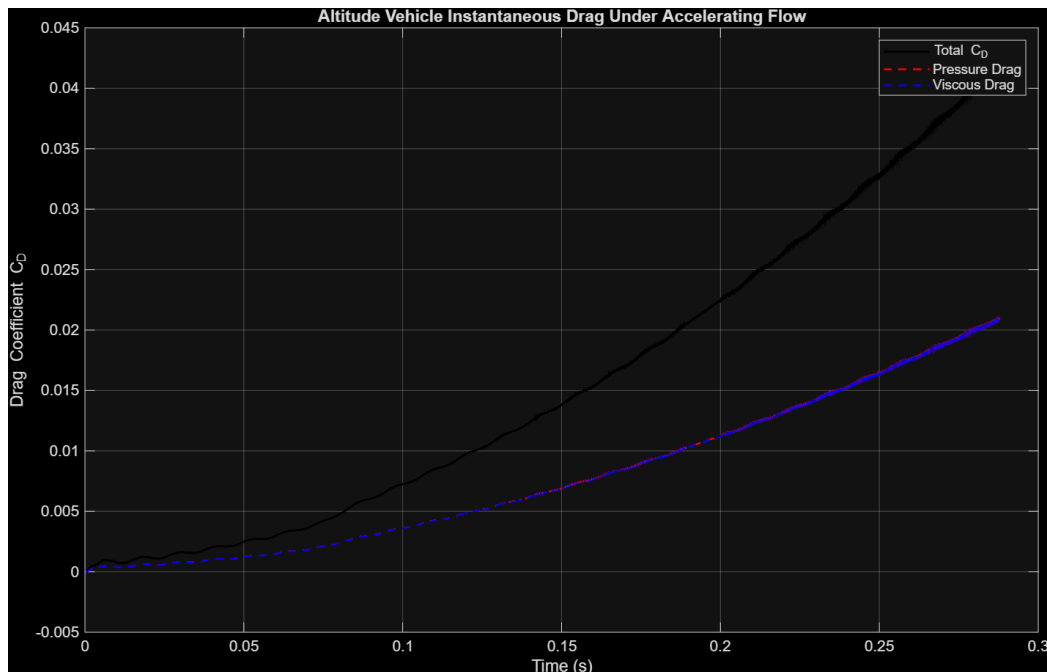


Fig. 7.23 .Instantaneous Drag Coefficient Evolution of Altitude Vehicle

Table 7.8. Mean Instantaneous Drag of Altitude Vehicle

Drag Quantities	Mean
Total Drag (C_D)	0.02268
Pressure Drag ($C_{D,p}$)	0.01136
Viscous Drag ($C_{D,v}$)	0.01133

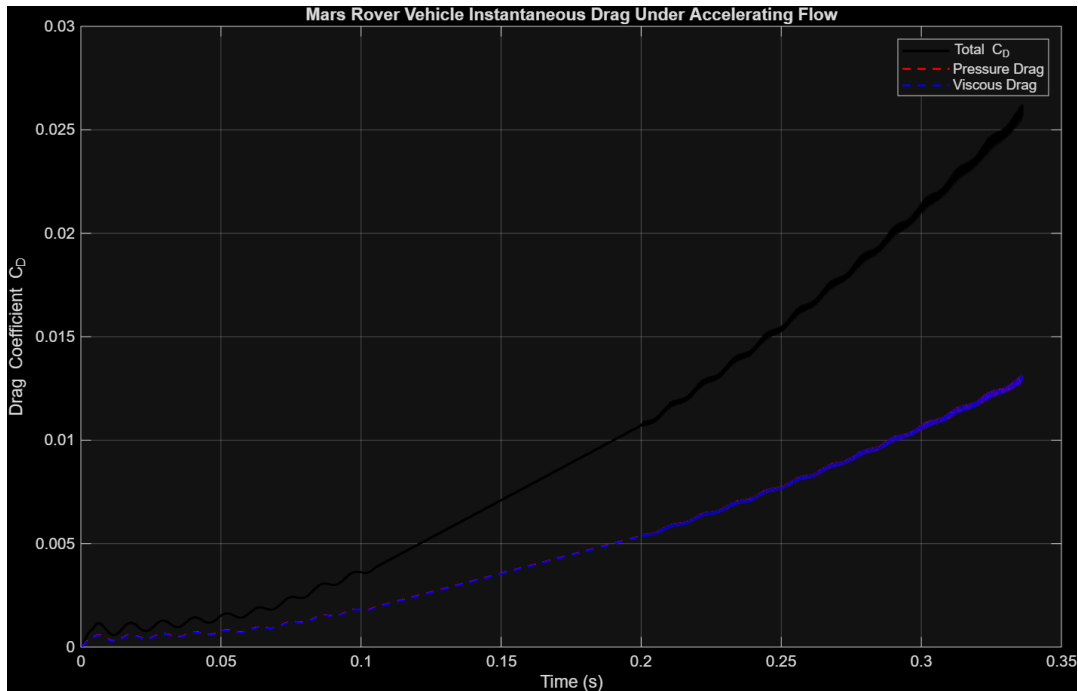


Fig. 7.24. Instantaneous Drag Coefficient Evolution of Mars Rover Vehicle

Table 7.9. Mean Instantaneous Drag of Mars Vehicle

Drag Quantities	Mean
Total Drag (C_D)	0.01622
Pressure Drag ($C_{D,p}$)	0.00812
Viscous Drag ($C_{D,v}$)	0.00810

7.2.5.7.2. Overall Drag Evolution

The instantaneous total drag coefficient for the both vehicles increase monotonically and nonlinearly over time as expected. This trend reflects the combined influence of increasing dynamic pressure and the unsteady development of the surrounding flow field. Unlike steady state drag curves evaluated at fixed Mach numbers, the drag here evolves continuously as freestream velocity increases, capturing rate-dependent aerodynamic response. It is key to observe that the rate of growth is convex upward, indicating that drag scales nonlinearly with velocity during acceleration.

7.2.5.7.3. Pressure vs. Viscous Drag Contributions

The total drag is composed of nearly equal pressure and viscous drag contributions. This indicates that pressure drag dominance is not overwhelming. This suggests that the vehicle geometry designs do not induce strong separation or large scale bluff body effects. In other words, the air flows smoothly around the body in a streamline fashion. However, in negative light the viscous drag remains significant since it nearly matches pressure drag. This indicates that even though flow flows in a streamline fashion, the skin-friction drag over the long slender body contributes substantially to total drag during acceleration.

7.2.5.7.4. Nonlinear Growth Mechanism

Even with the smooth prescribed acceleration, the drag scales quadratically. This is expected since $C_D \propto \frac{1}{2} \rho U^2$, and thus it is important to observe that there are no additional effects on drag besides the prescribed acceleration. It is also important to observe that even though the viscous drag is observed to be significant, the pressure drag slightly dominates. This indicates that geometry (vehicle shape) driven pressure forces govern the transient drag response. Nevertheless, the pressure drag increases smoothly as discussed earlier proving that our design manages the dominant drag contributor effectively during acceleration.

7.2.5.7.5. Engineering Interpretation

Insights discussed earlier conclude that the both vehicles positively exhibits:

- Predictable smooth drag growth. Drag behaves as expected from physical aerodynamics theory.
- No abrupt drag spikes. Indicates stable attached flow behavior
- Balanced drag mechanisms. The design avoids large transient penalties during acceleration.

7.2.5.7.6. Comparative Drag Behavior and Design Implications

Comparing both vehicle configurations under identical accelerating subsonic flow conditions reveal consistent trends in drag evolution, while also highlighting meaningful geometric effects on both magnitude and composition of aerodynamic drag. Both vehicles exhibit a monotonic nonlinear increase in drag during freestream acceleration and behave quadratically as expected. This trend reflects geometric influence on the drag quantities rather than numerical instability since both configurations have identical physical models, boundary conditions, and acceleration profiles.

Across the acceleration interval the Altitude vehicle consistently exhibits high instantaneous drag and thus a higher mean drag coefficient than the Mars Rover vehicle. The higher drag observed for the Altitude vehicle indicates greater sensitivity to pressure-driven aerodynamic loading. For both vehicles pressure drag dominates suggesting that neither vehicle behaves as a bluff body. This suggests that more importance needs to be given to the nose cone design and construction of the Altitude vehicle since pressure drag dominates and it is higher than that of the Mars Rover vehicle. As a result, it can be concluded that further optimization of the nose cone design without altering overall vehicle length that has proved a strong stability margin in earlier Rocksim simulated results discussions should result in a further reduction of drag. This is true since pressure drag is a culmination of mostly stagnation pressure at the tip of the vehicle suggesting room for optimization of the nose cone design of the Altitude vehicle.

7.2.5.8. Limitations/Future work

While the present study provided useful insight into the instantaneous drag response of the two vehicle configurations under accelerating subsonic flow, several limitations and room for future work should be acknowledged.

Although the prescribed acceleration rate was that of an estimated complete vehicular launch, the short acceleration interval of ~0.3 seconds compared to the estimated complete flight time of 8 seconds indicate that the flow does not reach a quasi-steady state equilibrium at any Mach number. The reported values provide rate-dependent insight that evolved over time rather than drag insight that outline the complete flight or insight that can be extrapolated/related to studying its effects at different Mach numbers.

Since no steady-state analysis was done, no steady-state data is available, and the simulation was not performed for long enough to reach a quasi-steady state directly comparing between instantaneous accelerating flow drag and corresponding steady-state drag at the same Mach number insight is not there. This limits the ability to quantify purely unsteady effects. Furthermore, since the force coefficients were normalized using an instantaneous freestream reference velocity, the reported drag coefficients are best interpreted comparatively and temporally rather than absolute values.

Although the mesh quality and numerical schemes were verified, the process was not thorough. Numerical residuals were not investigated leaving room for numerical noise. Formal mesh independence and time-step studies were not performed leaving room for mesh quality and time-step attached inaccurate results. Furthermore, the URANS turbulence model does not provide accurate wake dynamics data. Although details of that caliber are not significant in analysis such as this inaccuracies attached to the designed URANS model used can be present since URANS model sensitivity and independence study were not done.

Several extensions of the present study would provide a deeper physical insight. Extended time simulations to allow the acceleration phase to reach a constant velocity regime would allow direct comparison between acceleration flow drag and steady drag, to quantify purely unsteady drag effects. Varying the acceleration ramp rate would allow investigation of how strongly the drag depends on acceleration compared to steady flow at varying Mach numbers. A thorough verification and validation study of the results including that of sensitivity,

independence, and experimental results validation will increase reliability in results. Introducing varying angle of attack would extend relevance of the analysis to more realistic flight conditions assessing the coupling between acceleration and attitude induced aerodynamic loads.